mathematics

MDPI

Article

Qualitative Analysis for Modifying an Unstable Time-Fractional Nonlinear Schrödinger Equation: Bifurcation, Quasi-Periodic, Chaotic Behavior, and Exact Solutions

M. M. El-Dessoky [1,*], A. A. Elmandouh [2,3] and A. A. Alghamdi [1]

[1] Mathematics Department, Faculty of Science, King Abdulaziz University, P.O. Box 80203, Jeddah 21589, Saudi Arabia; aaalghamdi6@kau.edu.sa
[2] Department of Mathematics and Statistics, College of Science, King Faisal University, P.O. Box 400, Al-Ahsa 31982, Saudi Arabia; aelmandouh@kfu.edu.sa
[3] Department of Mathematics, Faculty of Science, Mansoura University, Mansoura 35516, Egypt
* Correspondence: mahmed4@kau.edu.sa

Abstract

This work explores the qualitative dynamics of the modified unstable time-fractional nonlinear Schrödinger equation (mUNLSE), a model applicable to nonlinear wave propagation in plasma and optical fiber media. By transforming the governing equation into a planar conservative Hamiltonian system, a detailed bifurcation study is carried out, and the associated equilibrium points are classified using Lagrange's theorem and phase-plane analysis. A family of exact wave solutions is then constructed in terms of both trigonometric and Jacobi elliptic functions, with solitary, kink/anti-kink, periodic, and super-periodic profiles emerging under suitable parameter regimes and linked directly to the type of the phase plane orbits. The validity of the solutions is discussed through the degeneracy property which is equivalent to the transmission between the phase orbits. The influence of the fractional derivative order on amplitude, localization, and dispersion is illustrated through graphical simulations, exploring the memory impacts in the wave evolution. In addition, an externally periodic force is allowed to act on the mUNLSE model, which is reduced to a perturbed non-autonomous dynamical system. The response to periodic driving is examined, showing transitions from periodic motion to quasi-periodic and chaotic regimes, which are further confirmed by Lyapunov exponent calculations. These findings deepen the theoretical understanding of fractional Schrödinger-type models and offer new insight into complex nonlinear wave phenomena in plasma physics and optical fiber systems.

Keywords: Schrödinger equations; bifurcation theory; phase portrait; quasi behaviour; chaotic pattern; wave solutions

MSC: 35C07; 35C08; 37K40; 83C15

Check for updates

Academic Editor: Fengping Yao

Received: 25 December 2025
Revised: 18 January 2026
Accepted: 19 January 2026
Published: 20 January 2026

Copyright: © 2026 by the authors. Licensee MDPI, Basel, Switzerland. This article is an open access article distributed under the terms and conditions of the Creative Commons Attribution (CC BY) license.

1. Introduction

Nonlinear phenomena appear in a wide range of scientific and engineering disciplines, including physics [1], engineering [2], applied mathematics [3], chemistry [4], and biology [5]. These phenomena are often modeled through nonlinear evolution equations (NLEEs). The significance of nonlinearity in wave dynamics has become increasingly evident in recent years, leading to substantial efforts aimed at developing analytical solutions for NLEE models [6,7]. Among the various nonlinear models, the nonlinear Schrödinger

equation (NLSE) stands out due to its broad applicability across numerous scientific domains. These include mathematical finance [8], optical fiber communications [9], fluid dynamics [10], quantum mechanics [11], plasma physics [12], quantum field theory [13], and wave propagation in piezoelectric materials [14]. Explicit solutions to NLEEs often exhibit soliton-like behavior, which plays a crucial role in modern technologies. In particular, solitons are fundamental in optical fiber systems for digital information transmission [15].

A key aspect of mathematical analysis in understanding the dynamics of nonlinear evolution equations (NLEEs) lies in constructing explicit solutions that accurately describe these processes. Over the past decades, significant efforts have been devoted to developing comprehensive analytical approaches for such models. Numerous mathematical techniques have been proposed and refined, including the generalized auxiliary equation technique [16,17], Kudryashov technique [18], classical Lie symmetry analysis [19,20], Hirota and modified Hirota bilinear method [21,22], sub-equation technique [23], extended direct algebraic technique [24], and bifurcation approach [25–29].

Within plasma physics and optical fiber research, nonlinear Schrödinger-type equations (NLSEs) provide a foundational modeling framework. A specific variant, known as the modified unstable nonlinear Schrödinger equation (mUNLSE), is particularly relevant for modeling phenomena such as two-layer baroclinic instability and symmetric two-stream plasma dynamics in lossless media. In this work, we investigate exact analytical solutions of the mUNLSE, formulated as follows [30]:

$$i\,{}_n\mathbb{D}_t^{\gamma,\nu}\,R + R_{xx} + 2\mu\,R|R|^2 + m\,{}_n\mathbb{D}_t^{\gamma,\nu}\left(R_x\right) = 0, \tag{1}$$

where $R(x,t)$ represents the complex-valued field envelope, x corresponds to the normalized longitudinal coordinate along the fiber, and t denotes the retarded time coordinate. Partial derivatives are expressed using subscript notation, and the parameter λ quantifies the strength of the self-phase modulation (SPM) effect. While ${}_n\mathbb{D}_t^{\gamma,\nu}(\cdot)$ for $\nu > 0$ and $\gamma \in (0,1]$, is the M-fractional derivative of order γ. The truncated M-fractional derivative used in Equation (1) belongs to a class of fractional operators that generalize classical definitions while preserving key properties of ordinary calculus, such as the product, quotient, and chain rules. The definition, main properties, and a detailed comparison with classical fractional operators are provided in Appendix A, in order to keep the article self-contained.

Fractional derivatives are widely used as modeling tools to achieve more accurate results in real-world applications. In the present problem, the nonlocal nature of the M-fractional derivative captures memory effects in wave propagation—the evolution at time t depends on previous states, a characteristic feature of fractional dynamics in plasmas and in optical fibers with hereditary behavior.

Equation (1) has been examined in a number of recent studies. For instance, the extended Jacobi elliptic function expansion and certain unified schemes have been employed to explore wave propagation and optical soliton dynamics in this setting [31]. In addition, an amended extended hyperbolic tangent approach was applied in [32] to analyze the solution structure of Equation (1). Furthermore, the MEM technique was utilized in [33] to construct optical soliton solutions of Equation (1). In [34,35], bright and dark soliton solutions, together with elliptic-function-type waves for the mUNLSE, were obtained via the modified extended direct algebraic method (MEDAM) and the simple equation method (SEM). A direct algebraic strategy was adopted in [36] to investigate the mUNLSE and its associated optical solitons, while a modified extended auxiliary equation mapping technique was proposed in [37] to derive soliton solutions for the mNLSE in fiber optics.

To the best of our knowledge, we note the following:

1. The lack of bifurcation studies, as well as analyses of quasi-periodic and chaotic behavior, for the time-fractional mUNLSE;
2. The importance of constructing exact solutions that are directly linked to phase-portrait structures through degeneracy analysis;
3. The insufficient exploration of the physical significance of memory effects and external perturbations in plasma and optical-fiber applications compared with purely soliton-based studies.

These gaps motivate us to further develop and complete the existing literature.

The paper is organized as follows: Section 2 presents the reduction of Equation (1) to a planar conservative dynamical system. Section 3 provides the bifurcation analysis and corresponding phase portraits. Section 4 introduces exact solutions to Equation (1). Section 5 illustrates graphical representations of the solutions and highlights the effect of the fractional derivative order. Section 6 investigates quasi-periodic behavior and chaotic patterns. Section 7 summarizes the key findings of the study.

2. Mathematical Analysis

We assume Equation (1) has a solution in the form

$$R(x,t) = e^{\mathrm{i}z}\Omega(\rho), \qquad z = p_1 x - \frac{q_1\Gamma(\nu+1)}{\gamma}t^{\gamma}, \qquad \rho = p_2 x - \frac{q_2\Gamma(\nu+1)}{\gamma}t^{\gamma}, \tag{2}$$

where p_i and q_i with $i = 1, 2$ are arbitrary constants while $\Omega(\rho)$ is a real valued function. Based on the properties of the truncated M-fractional derivative in Appendix A, we obtain

$$\begin{aligned} R_x &= e^{\mathrm{i}z}[\mathrm{i}p_1\Omega(\rho) + p_2\Omega'(\rho)], \\ R_{xx} &= e^{\mathrm{i}z}[p_2^2\Omega''(\rho) + 2\mathrm{i}p_1p_2\Omega'(\rho) - p_1^2\Omega(\rho)], \\ {}_n\mathbb{D}_t^{\gamma,\nu} R &= -e^{\mathrm{i}z}[q_2\Omega'(\rho) + \mathrm{i}q_1\Omega(\rho)], \\ {}_n\mathbb{D}_t^{\gamma,\nu} R_x &= -e^{\mathrm{i}z}[-p_2q_2\Omega''(\rho) - \mathrm{i}(p_1q_2 + p_2q_1)\Omega'(\rho) + q_1p_1\Omega]. \end{aligned} \tag{3}$$

Inserting the expression (3) into Equation (1) and separating the real and imaginary parts gives the following:

Real part:

$$p_2(p_2 - mq_2)\Omega''(\rho) + 2\mu\Omega^3(\rho) + (mp_1q_1 - p_1^2 + q_1)\Omega(\rho) = 0. \tag{4}$$

Imaginary part:

$$[m(p_1q_2 + p_2q_1) - 2p_1p_2 + q_2]\Omega'(\rho) = 0. \tag{5}$$

Equation (5) is identically verified if

$$m = \frac{2p_1p_2 - q_2}{p_1q_2 + p_2q_1}. \tag{6}$$

Inserting the expression (6) into Equation (4) implies

$$\Omega'' - \ell_1\Omega^3(\rho) + \ell_2\Omega(\rho) = 0, \tag{7}$$

where ℓ_1 and ℓ_2 are new constants introduced for simplicity and they are given by

$$\ell_1 = \frac{2\mu(p_1q_2 + p_2q_1)}{p_2(p_1p_2q_2 - p_2^2q_1 - q_2^2)}, \qquad \ell_2 = \frac{p_1^3q_2 - p_1^2p_2q_1 - p_2q_1^2}{p_2(p_1p_2q_2 - p_2^2q_1 - q_2^2)}. \tag{8}$$

Defining $\Omega' = \Upsilon(\rho)$, Equation (7) reduces to a two-dimensional dynamical system in the form

$$\begin{aligned} \Omega' &= \Upsilon \\ \Upsilon' &= \ell_1\Omega^3 - \ell_2\Omega. \end{aligned} \tag{9}$$

The dynamical system (9) is conservative because $\mathrm{div}(\Omega', \Upsilon') = 0$. Moreover, it is Hamiltonian because it can be obtained from the Hamilton function

$$H = \frac{1}{2}\Upsilon^2 - \frac{\ell_1}{4}\Omega^4 + \frac{\ell_2}{2}\Omega^2, \tag{10}$$

by using Hamilton canonical equations [38]. Due to $\partial_\rho H = 0$, the Hamilton function (10) itself is a conserved quantity, i.e., it has a constant value along any trajectories. Thus, we have

$$H = \frac{1}{2}\Upsilon^2 - \frac{\ell_1}{4}\Omega^4 + \frac{\ell_2}{2}\Omega^2 = a, \tag{11}$$

where a is free parameter. The Hamiltonian (11) is elucidated physically via the 1D motion of a unit mass particle under the impact of two parameters' potential functions in the form

$$V(\Omega) = -\frac{\ell_1}{4}\Omega^4 + \frac{\ell_2}{2}\Omega^2. \tag{12}$$

Hence, the solution of the Hamiltonian system (9) is obtained by quadrature, and consequently, we obtain the solution to Equation (1). Inserting the first equation in Equation (9) into Equation (11) and separating the variables gives

$$\pm\sqrt{2}\mathrm{d}\rho = \frac{\mathrm{d}\Omega}{\sqrt{G_4(\Omega)}}, \tag{13}$$

where the quartic polynomial $G_4(\Omega)$ is given by

$$G_4(\Omega) = a - \frac{\ell_2}{2}\Omega^2 + \frac{\ell_1}{4}\Omega^4. \tag{14}$$

To integrate both sides of Equation (13), we must find the range of the parameters a, ℓ_1, ℓ_2 and the intervals of the real solution because $\Omega(\rho)$ is real valued function. The phase portrait analysis for the system (9) is investigated not only to determine this range of the parameters but also because it provides the types of the solution before constructing them.

3. Qualitative Analysis

In this section, we examine the qualitative dynamics of the Hamiltonian system (9) by means of its phase portrait and investigate the nature of the corresponding trajectories using the Hamiltonian concepts. The equilibrium points of system (9) arise as the critical points to the potential function (12), i.e., they are $\Omega_0, 0$, where Ω_0 is a solution to $\partial_\Omega V(\Omega_0) = \Omega_0(\ell_2 - \ell_1\Omega_0^2) = 0$. When $\ell_1\ell_2 < 0$, the system possesses a single equilibrium point, namely the trivial solution at the origin, $O = (0, 0)$. Conversely, if $\ell_1\ell_2 > 0$ with $\ell_1 \neq 0$, three distinct equilibrium points emerge: the origin together with two symmetric nontrivial equilibria, $O = (0, 0)$, $C_{1,2} = \left(\pm\sqrt{\frac{\ell_2}{\ell_1}}, 0\right)$. To specify the nature these equilibria, we proceed by applying Lagrange's theorem [39], which states that the isolated equilibrium point is either stable or unstable if it is either the minimum or maximum point of the potential function. Therefore, we compute $\partial_{\Omega\Omega}V$ at the equilibrium points. Hence, we have

$$\partial_{\Omega\Omega}V|_{\Omega=0} = \ell_2, \qquad \partial_{\Omega\Omega}V|_{\Omega=\pm\sqrt{\frac{\ell_2}{\ell_1}}} = -2\ell_2. \tag{15}$$

Following Lagrange's theorem [39], the equilibrium point O is classified as a center when $\ell_2 > 0$ and $\ell_1 < 0$, whereas it becomes a saddle point when $\ell_2 < 0$ and $\ell_1 > 0$. In the case $\ell_2 < 0$ and $\ell_1 < 0$, the origin O is a saddle, while the two nontrivial equilibria $C_{1,2}$ are centers. Conversely, if $\ell_2 > 0$ and $\ell_1 > 0$, the origin O is a center and the equilibria $C_{1,2}$ are saddles. Figure 1 describes the phase portrait for the system (9).

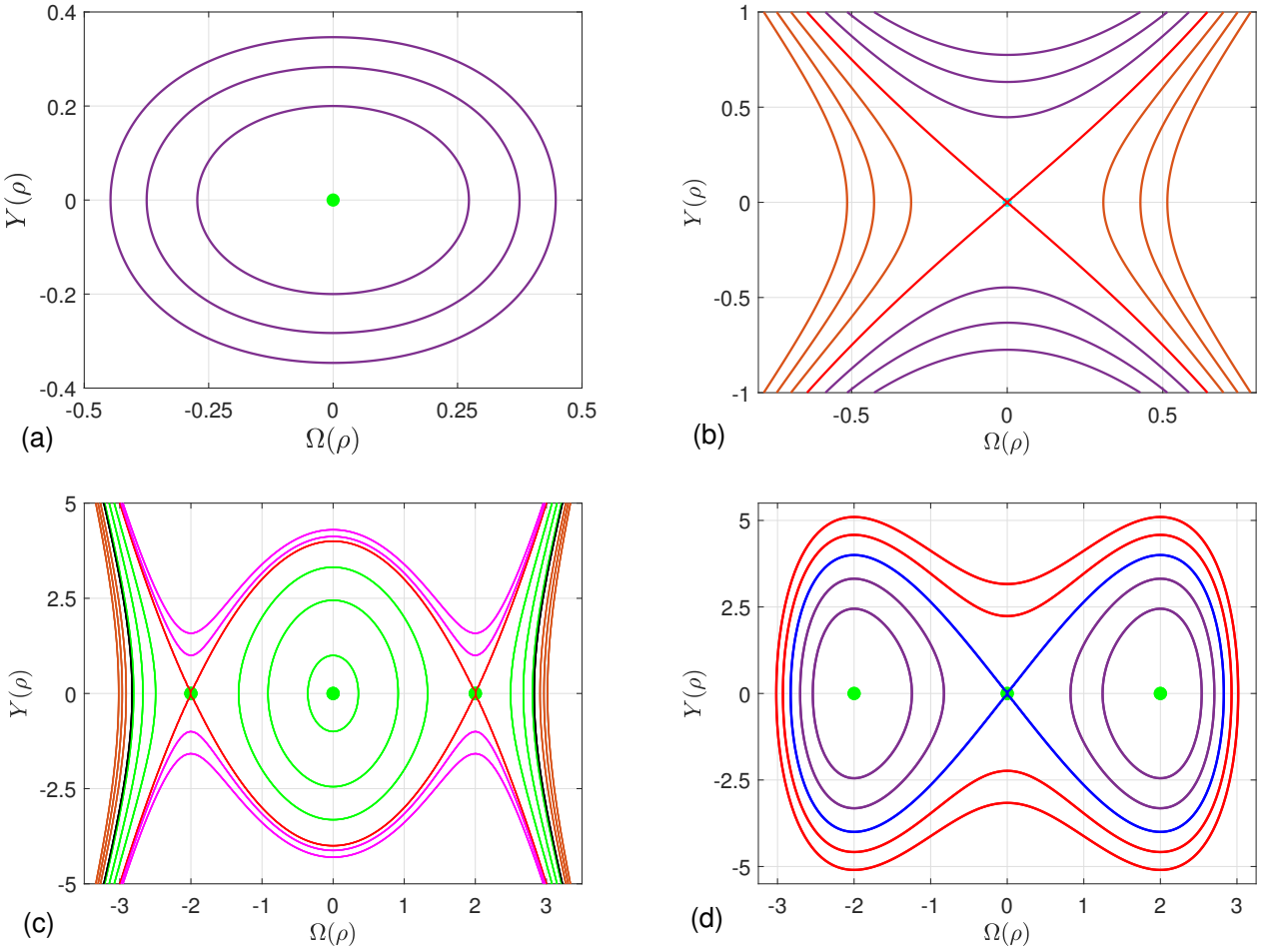


Figure 1. Phase portraits for system (9): (**a**) $\ell_1 < 0, \ell_2 > 0$; (**b**) $\ell_1 > 0, \ell_2 < 0$; (**c**) $\ell_1 > 0, \ell_2 > 0$; (**d**) $\ell_1 < 0, \ell_2 < 0$.

To describe the phase portrait more concretely, we compute the energy levels at the equilibrium points:

$$a_1 = H(O) = 0, \qquad a_2 = H(C_{1,2}) = \frac{{\ell_2}^2}{4\ell_1}. \tag{16}$$

To provide a more concrete description of the phase portrait, we first evaluate the energy levels at the equilibrium points:

$$\mathcal{N}_a = \left\{ (\Omega, \Upsilon) \in \mathbb{R} \times \mathbb{R} : \tfrac{1}{2}\Upsilon^2 = F_4(\Omega) \right\}. \tag{17}$$

In the phase portrait of system (9), every trajectory is associated with an energy level curve defined by its corresponding energy value.

We now provide a qualitative description of the phase portraits associated with system (9).

(A) For $\ell_1 < 0$ and $\ell_2 > 0$, the system admits a single equilibrium point at the origin O, which behaves as a center. When the energy level satisfies $a > 0$, the trajectories form

a continuous family of closed periodic curves, denoted by $\{\mathcal{N}_a : a > 0\}$, encircling the center O. This configuration is illustrated in Figure 1a.

(B) For $\ell_1 > 0$ and $\ell_2 < 0$, the origin O becomes a saddle equilibrium. At the critical energy level $a = 0$, the system supports a distinguished unbounded trajectory (highlighted in red), denoted by $\mathcal{N}_{a=0}$, as shown in Figure 1b. For $a > 0$, the dynamics give rise to a family of unbounded trajectories (depicted in purple), $\{\mathcal{N}_a : a > 0\}$. Conversely, for $a < 0$, another family of unbounded trajectories (depicted in gold) emerges. As the energy approaches zero, both families (purple and gold) converge to the unique orbit $\mathcal{N}_{a=0}$.

(C) For $\ell_1 > 0$ and $\ell_2 > 0$, the dynamical system (9) admits three equilibrium points: two saddles and one center, as depicted in Figure 1c. At $a = 0$, the system generates a black unbounded trajectory with a hyperbolic profile in addition to the equilibrium point O. When $a < 0$, it produces a gold family of unbounded orbits, all sharing the same hyperbolic geometry. Within the interval $0 < a < a_2$, a green family of solutions emerges, consisting of two distinct parts: one bounded by the heteroclinic curve $\mathcal{N}_{a=a_2}$ (shown in red), and another with hyperbolic form. For $a > a_2$, the system displays a pink family of unbounded trajectories. As $a \to 0$, the gold family collapses into the black unbounded orbit, while the hyperbolic branch of the green family also converges to the same black orbit. Meanwhile, the periodic green family enclosed by the heteroclinic orbit contracts to the equilibrium point O. As $a \to a_2$, the pink unbounded family is absorbed into the red heteroclinic orbit, and the green family likewise transitions into the red heteroclinic structure.

(D) For $\ell_1 < 0$ and $\ell_2 < 0$, system (9) admits three equilibrium points: one saddle and two centers, as illustrated in Figure 1d. At the energy level $a = 0$, the system exhibits a homoclinic trajectory (shown in blue) that departs from the saddle point O and returns to it. For intermediate values $a_2 < a < 0$, two distinct families of closed periodic trajectories (depicted in purple) appear inside the homoclinic loop. When $a > 0$, the dynamics reduce to a single family of bounded periodic trajectories.

4. Solution Construction

The purpose of this section is to obtain bounded wave solutions of Equation (1). These solutions can be classified into three main types: solitary waves, kink (or anti-kink) waves, and periodic waves. Although the adopted method is sufficiently general to construct unbounded solutions, such cases are excluded here because they are not physically relevant. For clarity in the forthcoming analysis, the conditions that lead to periodic, super-periodic, solitary, and homoclinic solutions are summarized in Table 1. This organization highlights the correspondence between the wave forms of system (9) and the nature of their phase trajectories: periodic and super-periodic waves arise from periodic and super-periodic phase orbits, solitary waves are associated with homoclinic orbits, and kink (or anti-kink) waves originate from heteroclinic orbits.

Table 1. Existence and classification of the solutions.

Case	ℓ_1	ℓ_2	a	Figure/Orbit Color	Solution's Type
1.	$-$	$-$	0	Figure 1d/blue	Solitary
2.	$+$	$+$	a_2	Figure 1c/red	Kink(anti-kink)
3.	$-$	$+$	$+$	Figure 1a/purple	periodic
4.	$+$	$+$	$(0, a_2)$	Figure 1c/green	periodic
5.	$-$	$-$	$(a_2, 0)$	Figure 1d/purple	periodic
6.	$-$	$-$	$+$	Figure 1d/red	Super-periodic

Proceeding to integrate the differential form given in (13), we apply the parameter conditions summarized in Table 1 to identify admissible solutions.

4.1. Solitary Solution

The condition listed in the first row of Table 1 corresponds to the existence of a solitary-wave solution. We now construct this solution explicitly. When the parameters ℓ_1, ℓ_2, and a satisfy the third condition of first row of Table 1, system (9) possesses two blue homoclinic orbits that cross the Ω-axis at three distinct points, as shown in Figure 1d. Consequently, the polynomial $F_4(\Omega)$ admits four real roots: a double root at the origin and two simple roots at $\Omega = \pm\sqrt{2\ell_2/\ell_1}$. Hence, $F_4(\Omega)$ can be written as $F_4(\Omega) = -\frac{\ell_1}{4}\Omega^2\left(\frac{2\ell_2}{\ell_1} - \Omega^2\right)$. For a real-valued solution we require $\Omega \in \left(-\sqrt{\frac{2\ell_2}{\ell_1}},\ 0\right) \cup \left(0,\ \sqrt{\frac{2\ell_2}{\ell_1}}\right)$. Setting the initial condition $\Omega(\rho_0) = \pm\sqrt{2\ell_2/\ell_1}$ and integrating (13) gives the solitary-wave profile

$$\Omega(\rho) = \pm\sqrt{\frac{2\ell_2}{\ell_1}}\operatorname{sech}\left(\sqrt{-\ell_2}\,(\rho - \rho_0)\right). \tag{18}$$

Using both Equations (2) and (18) produces a new solution to Equation (1) in the form

$$R(x,t) = \pm\sqrt{\frac{2\ell_2}{\ell_1}}e^{\mathrm{i}\left(p_1 x - \frac{q_1\Gamma(\nu+1)}{\gamma}t^\gamma\right)}\operatorname{sech}\left(\sqrt{-\ell_2}\,\left(p_2 x - \frac{q_2\Gamma(\nu+1)}{\gamma}t^\gamma - \rho_0\right)\right). \tag{19}$$

4.2. Kink (Anti-Kink) Solution

The second row outlined in Table 1 guarantees that a heteroclinic orbit links the saddle equilibria C_1 and C_2, indicating the possibility of kink/anti-kink wave solutions. We now derive this solution explicitly. When the parameters ℓ_1, ℓ_2, and a meet the criterion of the second row, system (9) supports a red heteroclinic trajectory (see Figure 1c), which intersects the Ω-axis at two locations. Accordingly, the polynomial $F_4(\Omega)$ possesses a pair of double roots at $\Omega = \pm\sqrt{\ell_2/\ell_1}$, allowing it to be factored as $F_4(\Omega) = \frac{\ell_1}{4}\left(u^2 - \frac{\ell_2}{\ell_1}\right)^2$. Real solutions are restricted to the intervals $\Omega \in \left(-\sqrt{\frac{\ell_2}{\ell_1}},\ 0\right) \cup \left(0,\ \sqrt{\frac{b}{a}}\right)$. Choosing the initial condition $\Omega(\rho_0) = 0$ and integrating (13) yields the kink profile

$$\Omega(\rho) = \pm\sqrt{\frac{\ell_2}{\ell_1}}\tanh\left(\sqrt{\frac{\ell_2}{2}}\,(\rho - \rho_0)\right). \tag{20}$$

Substituting this result into Equation (2) givesa new solution to Equation (1) in the form

$$R(x,t) = \pm\sqrt{\frac{\ell_2}{\ell_1}}e^{\mathrm{i}\left(p_1 x - \frac{q_1\Gamma(\nu+1)}{\gamma}t^\gamma\right)}\tanh\left(\sqrt{\frac{\ell_2}{2}}\,\left(p_2 x - \frac{q_2\Gamma(\nu+1)}{\gamma}t^\gamma - \rho_0\right)\right). \tag{21}$$

4.3. Periodic Solution

We consider the third, fourth, and fifth rows of Table 1 individually.

(i) If the parameters satisfy $\ell_1 < 0$, $\ell_2 > 0$, and $a > 0$, the phase portrait of system (9) contains a periodic orbit encircling the equilibrium O. This closed trajectory meets the Ω-axis at two distinct points, implying that the associated polynomial $F_4(\Omega)$ has two real roots and a pair of complex-conjugate roots. It can therefore be written in the factorized form $F_4(\Omega) = -\frac{\ell_1}{4}\left(\vartheta_1^2 - \Omega^2\right)\left(\vartheta_2^2 + \Omega^2\right)$. A real-valued solution is admissible only for Ω lying in the open interval $(-\vartheta_1,\ \vartheta_2)$. Setting the initial condition $\Omega(\rho_0) = \vartheta_1$ and integrating Equation (9) leads to the periodic solution expressed via the Jacobi elliptic cosine:

$$\Omega(\rho) = \vartheta_1 \mathrm{cn}\left(\sqrt{\frac{-\ell_1\left(\vartheta_1^2+\vartheta_2^2\right)}{2}}\,(\rho-\rho_0),\ \frac{\vartheta_1}{\sqrt{\vartheta_1^2+\vartheta_2^2}}\right). \tag{22}$$

Substituting this result into Equation (2) results in a new solution to Equation (1) in the form

$$R(x,t) = \vartheta_1 e^{\mathrm{i}\left(p_1 x - \frac{q_1\Gamma(\nu+1)}{\gamma}t^\gamma\right)} \mathrm{cn}\left(\sqrt{\frac{-\ell_1\left(\vartheta_1^2+\vartheta_2^2\right)}{2}}\,\left(p_2 x - \frac{q_2\Gamma(\nu+1)}{\gamma}t^\gamma - \rho_0\right),\ \frac{\vartheta_1}{\sqrt{\vartheta_1^2+\vartheta_2^2}}\right). \tag{23}$$

(ii) When the parameters are chosen such that $\ell_1 < 0$, $\ell_2 < 0$, and $a_2 < a < 0$, system (9) admits a pair of green periodic orbits (see Figure 1d), each crossing the Ω-axis at four distinct locations. Consequently, the polynomial $F_4(\Omega)$ possesses four real roots, which we denote by $\pm\vartheta_3$ and $\pm\vartheta_4$ with $0 < \vartheta_3 < \vartheta_4$. It can therefore be factored as $F_4(\Omega) = -\frac{\ell_1}{4}\left(\Omega^2-\vartheta_3^2\right)\left(\vartheta_4^2-\Omega^2\right)$. Real, bounded solutions are confined to the intervals $\Omega \in \left(-\vartheta_4,-\vartheta_3\right)\cup\left(\vartheta_3,\vartheta_4\right)$. Taking the initial condition $\Omega(\rho_0) = \pm\vartheta_4$ and integrating (13) produces the solution in terms of the Jacobi elliptic dn function:

$$\Omega(\rho) = \pm\vartheta_4 \mathrm{dn}\left(\vartheta_4\sqrt{\frac{-\ell_1}{2}}(\rho-\rho_0),\ \frac{\sqrt{\vartheta_4^2-\vartheta_3^2}}{\vartheta_4}\right). \tag{24}$$

Using both Equations (2) and (24) produces a new solution to Equation (1) in the form

$$R(x,t) = \pm\vartheta_4 e^{\mathrm{i}\left(p_1 x - \frac{q_1\Gamma(\nu+1)}{\gamma}t^\gamma\right)} \mathrm{dn}\left(\vartheta_4\sqrt{\frac{-\ell_1}{2}}\left(p_2 x - \frac{q_2\Gamma(\nu+1)}{\gamma}t^\gamma - \rho_0\right),\ \frac{\sqrt{\vartheta_4^2-\vartheta_3^2}}{\vartheta_4}\right). \tag{25}$$

(iii) When the parameters are fixed with $\ell_1 > 0$, $\ell_2 > 0$, and $a_2 < a < 0$, system (9) displays three distinct trajectories: a single periodic orbit together with two families of unbounded orbits. Correspondingly, the polynomial $F_4(\Omega)$ admits four simple real roots, which we label as $\pm\vartheta_5$ and $\pm\vartheta 6$, ordered such that $0 < \vartheta_5 < \vartheta_6$. It therefore factors as $F_4(\Omega) = \frac{\ell_1}{4}\left(\Omega^2-\vartheta_5^2\right)\left(\Omega^2-\vartheta_6^2\right)$. Bounded, real-valued solutions are only possible for Ω in the disjoint intervals $\Omega \in (-\vartheta_5, 0)\cup(0,\vartheta_5)$. Imposing the initial condition $\Omega(\rho_0) = 0$ and integrating (13) leads to a solution expressed by the Jacobi elliptic sine function:

$$\Omega(\rho) = \pm\vartheta_5 \mathrm{sn}\left(\vartheta_6\sqrt{\frac{\ell_1}{2}}\,(\rho-\rho_0),\ \frac{\vartheta_5}{\vartheta_6}\right). \tag{26}$$

Using both Equations (2) and (26) provides a new solution to Equation (1) in the form

$$R(x,t) = \pm\vartheta_5 e^{\mathrm{i}\left(p_1 x - \frac{q_1\Gamma(\nu+1)}{\gamma}t^\gamma\right)} \mathrm{sn}\left(\vartheta_6\sqrt{\frac{\ell_1}{2}}\,\left(p_2 x - \frac{q_2\Gamma(\nu+1)}{\gamma}t^\gamma - \rho_0\right),\ \frac{\vartheta_5}{\vartheta_6}\right). \tag{27}$$

4.4. Super-Periodic Solution

The last row in Table 1 refers to the existence of a super-periodic wave solution to Equation (1). Under parameter values ℓ_1, ℓ_2, and a that fulfill this condition, the phase portrait of system (9) contains a red super-periodic orbit (Figure 1d), which meets the Ω-axis at two locations. This geometric feature implies that the associated polynomial $F_4(\Omega)$ possesses a pair of real roots, $\pm\vartheta_7$, together with a pair of purely imaginary conjugate roots, $\pm\mathrm{i}\vartheta_8$. Consequently, the polynomial factors as $F_4(\Omega) = -\frac{\ell_1}{4}\left(\vartheta_7^2-\Omega^2\right)\left(\Omega^2+\vartheta_8^2\right)$.

A physically relevant (real) solution is obtained only when Ω lies in the open interval $(-\vartheta_7, \vartheta_7)$. Choosing the initial value $\Omega(\rho_0) = \vartheta_7$ and integrating (13) gives the super-periodic profile, in terms of the Jacobi elliptic cosine,

$$\Omega(\rho) = \pm\vartheta_7 \mathrm{cn}\left(\sqrt{\frac{-\ell_1\left(\vartheta_7^2+\vartheta_8^2\right)}{2}}\,(\rho-\rho_0),\ \frac{\vartheta_7}{\sqrt{\vartheta_7^2+\vartheta_8^2}}\right). \tag{28}$$

Substituting this expression into Equation (2) yields

$$R(x,t) = \pm\vartheta_7 e^{\mathrm{i}(p_1 x - \frac{q_1\Gamma(\nu+1)}{\gamma}t^\gamma)} \mathrm{cn}\left(\sqrt{\frac{-\ell_1\left(\vartheta_7^2+\vartheta_8^2\right)}{2}}\,(p_2 x - \frac{q_2\Gamma(\nu+1)}{\gamma}t^\gamma - \rho_0),\ \frac{\vartheta_7}{\sqrt{\vartheta_7^2+\vartheta_8^2}}\right). \tag{29}$$

The solution (29) is a new solution to Equation (1).

4.5. Solution Validity

This subsection verifies the consistency and validity of the derived solutions using the degeneracy property. This property is defined by the study of solution degeneracy through the phase orbit transition for limiting values of the bifurcation parameter a.

I. As the parameter a tends to zero, the family of blue periodic orbits shown in Figure 1a contracts toward the equilibrium point at the origin, O. In this limit, the root ϑ_1 approaches zero, causing solution (22) to vanish. The zero value corresponds to the Ω-coordinate of the equilibrium O. Furthermore, solution (23) reduces to $R(x,t) = 0$, which is the trivial solution of Equation (1).

II. In the limit $a \to 0^-$, the family of purple periodic orbits deforms continuously into the blue homoclinic orbits, as illustrated in Figure 1d. Hence, we have $\vartheta_3 = 0$ and $\vartheta_4 = \sqrt{2\ell_2/\ell_1}$. As a result, the periodic solution given in (25) reduces to the solitary-wave profile described by Equation (19).

III. In the limit $a \to 0^+$, the red super-periodic orbits merge into the blue homoclinic orbit depicted in Figure 1d. In this limit, the parameters become $\vartheta_7 = \sqrt{2\ell_2/\ell_1}$ and $\vartheta_8 = 0$. As a result, solution (29) simplifies to the form:

$$\begin{aligned} R(x,t) &= \pm\vartheta_7 e^{\mathrm{i}(p_1 x - \frac{q_1\Gamma(\nu+1)}{\gamma}t^\gamma)} \mathrm{cn}\left(\sqrt{\frac{-\ell_1\left(\vartheta_7^2+\vartheta_8^2\right)}{2}}\,(p_2 x - \frac{q_2\Gamma(\nu+1)}{\gamma}t^\gamma - \rho_0),\ 1\right), \\ &= \pm\sqrt{\frac{2\ell_2}{e^{\mathrm{i}(p_1 x - \frac{q_1\Gamma(\nu+1)}{\gamma}t^\gamma)}\ell_1}}\,\mathrm{sech}\left(\sqrt{-\ell_2}\,(p_2 x - \frac{q_2\Gamma(\nu+1)}{\gamma}t^\gamma - \rho_0)\right), \end{aligned} \tag{30}$$

which is in agreement with the solution in Equation (19).

IV. As the parameter limit is approached to a_2, the green periodic orbits continuously deform into the red heteroclinic orbit shown in Figure 1c. In this degenerate case, the two roots coincide, giving $\vartheta_5 = \vartheta_6 = \sqrt{\ell_2/\ell_1}$. Consequently, the periodic solution (27) collapses to

$$\begin{aligned} R(x,t) &= \pm\sqrt{\ell_2/\ell_1} e^{\mathrm{i}(p_1 x - \frac{q_1\Gamma(\nu+1)}{\gamma}t^\gamma)} \mathrm{sn}\left(\sqrt{\frac{\ell_2}{2}}\,(p_2 x - \frac{q_2\Gamma(\nu+1)}{\gamma}t^\gamma - \rho_0),\ 1\right), \\ &= \pm\sqrt{\frac{\ell_2}{\ell_1}} e^{\mathrm{i}(p_1 x - \frac{q_1\Gamma(\nu+1)}{\gamma}t^\gamma)} \tanh\left(\sqrt{\frac{\ell_2}{2}}\,(p_2 x - \frac{q_2\Gamma(\nu+1)}{\gamma}t^\gamma - \rho_0)\right), \end{aligned} \tag{31}$$

which is in agreement with the solution (21).

Hence, the degeneracy property confirms the consistency and validity of the obtained analytical result.

5. Graphical Representation

The purpose of this section is to present graphical interpretations of the derived solutions and to highlight how fractional derivatives influence their behavior.

We arbitrarily assume $\mu = 0.2,\ p_1 = -0.3,\ p_2 = -0.5,\ q_1 = -0.08,\ q_2 = -0.07$. Substituting these values into Equations (6) and (8) yields

$$m = 6.06557377, \qquad \ell_1 = -10.60869565, \qquad \ell_2 = -0.6478260870.$$

Since $(\ell_1, \ell_2) \in \mathbb{R}^- \times \mathbb{R}^-$, the corresponding phase portrait of system (9) is shown in Figure 1d. The solution of Equation (1) is then determined by the value of parameter a. Accordingly, we consider the following three cases:

A. If $a = 0$, Equation (1) has a solution in the form

$$R(x,t) = 0.3494726707\, e^{\left(-0.3x + \frac{0.08\Gamma(\nu+1)t^{\gamma}}{\gamma}\right)i} \operatorname{sech}\left(0.402438221x - \frac{0.05634135095\Gamma(\nu+1)t^{\gamma}}{\gamma} + \rho_0\right). \tag{32}$$

Figure 2 displays the behavior of the real component of the solution $R(x,t)$ associated with Equation (19). In panel (a), a three-dimensional surface representation of Re.$R(x,t)$ is shown over the (x,t)-plane. The profile forms a sharply localized solitary wave centered near $x = 0$, with its amplitude decreasing rapidly as one moves away from the center, illustrating strong spatial confinement and stable propagation characteristics. Figure 2b depicts the temporal evolution of Re.$R(2,t)$ at the fixed spatial location $x = 2$ for several choices of the fractional derivative order γ. The red curve corresponds to the classical limit $\gamma = 1$, while the green and blue curves illustrate the fractional cases $\gamma = 0.7$ and $\gamma = 0.4$, respectively. A reduction in the fractional order leads to a broader temporal profile and a noticeably slower decay rate, a behavior consistent with the increased memory effects inherent to fractional operators. These observations emphasize how sensitively the wave amplitude, temporal dispersion, and long-time persistence depend on the value of γ.

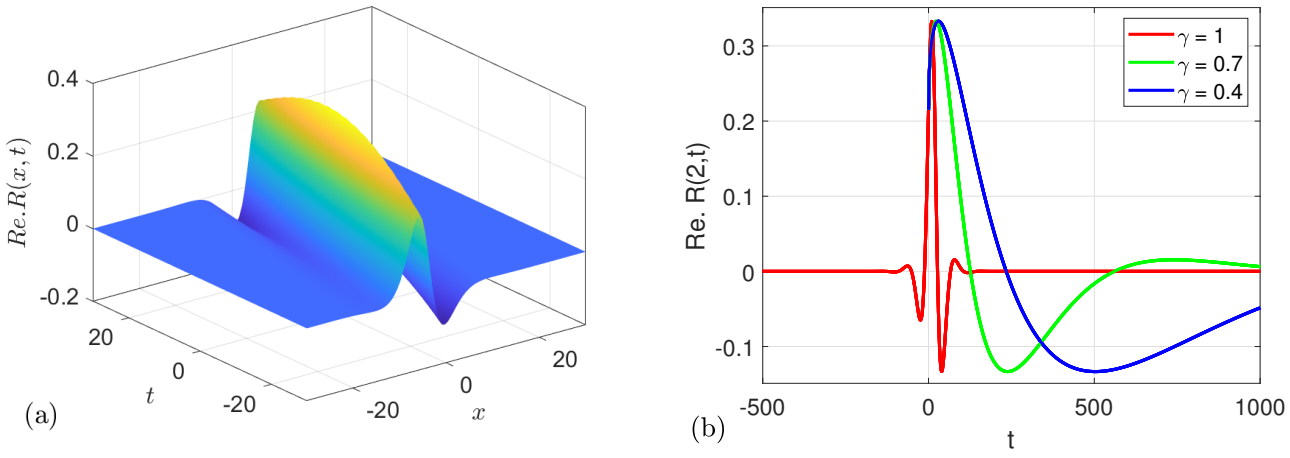


Figure 2. Graphic representation to the real part of the solution (19). (**a**) 3D-representation (**b**) 2D representation for different values of the fractional order derivative.

B. If $a = -0.004944983965 \in ({\ell_2}^2/(4\ell_1), 0) = (-0.009889967930, 0)$, Equation (1) has a solution:

$$R(x,t) = 0.3228706477e^{i\left(0.3x-\frac{0.08\Gamma(\nu+1)t^{\gamma}}{\gamma}\right)}\,\mathrm{dn}\left(0.3718044356x-\frac{0.05205262098\Gamma(\nu+1)t^{\gamma}}{\gamma}\right.$$
$$\left.,0.9101797209\right). \tag{33}$$

Figure 3 illustrates the real part of solution (33). Figure 3a presents a 3D surface of Re.$R(x,t)$, showing a localized wave profile with a pronounced peak and rapid spatial decay. Figure 3b displays the time evolution of Re.$R(2,t)$ for different fractional orders γ. As γ decreases from 1 to 0.4, the waveform broadens and decays more slowly, reflecting the effects in the fractional model.

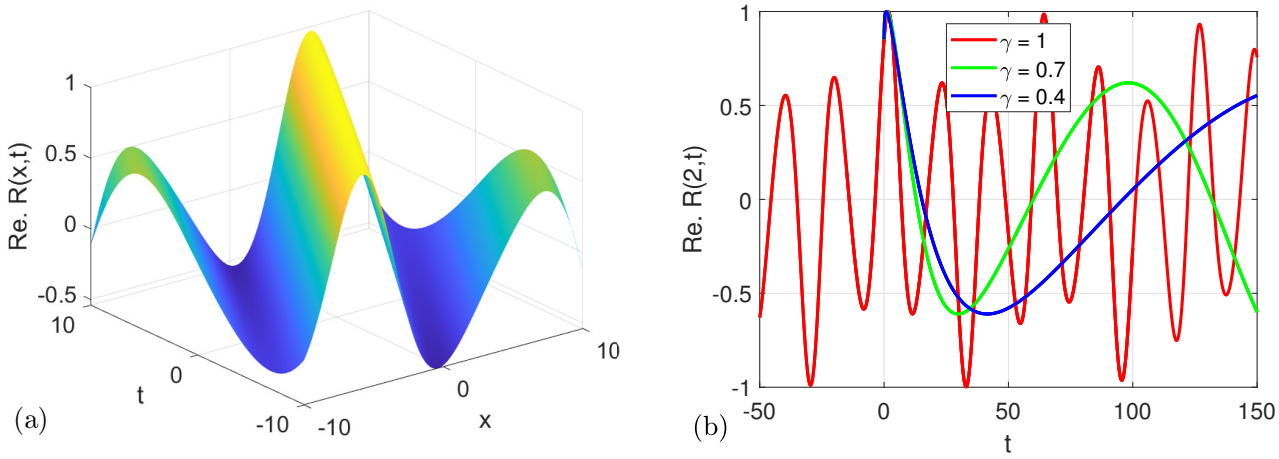


Figure 3. Graphic representation of the real part of the solution (25). (**a**) The 3D representation and (**b**) 2D representation for different values of the fractional order derivative.

C. If $a = 0.9901100321 > 0$, Equation (1) has a solution in the form

$$R(x,t) = 0.8225723213e^{i\left(0.3x-\frac{0.08\Gamma(\nu+1)t^{\gamma}}{\gamma}\right)}\,\mathrm{cn}\left(1.277721114x-\frac{0.1788809559\Gamma(\gamma+1)t^{\nu}}{\gamma}\right.$$
$$\left.,0.7413512465\right). \tag{34}$$

Figure 4 illustrates the real part of solution (34). Figure 4a shows a three-dimensional surface plot of Re.$R(x,t)$, revealing a localized wave structure whose amplitude varies in both space and time. Figure 4b presents the temporal evolution of Re.$R(2,t)$ at the fixed point $x = 2$ for several fractional orders γ. The curves corresponding to $\gamma = 1$, $\gamma = 0.7$, and $\gamma = 0.4$ demonstrate that decreasing the fractional order leads to slower decay and broader temporal spreading, reflecting the enhanced memory effects inherent to fractional derivatives.

Hence, physically, γ characterizes memory and nonlocal temporal effects. In plasma media, it accounts for anomalous transport and long-range particle interactions, whereas in optical fibers it reflects delayed nonlinear responses and dispersive memory effects. As illustrated in Figures 2–4, decreasing γ leads to slower decay, broader temporal spreading, and enhanced wave persistence, thereby demonstrating the direct physical influence of fractional dynamics on wave localization and stability.

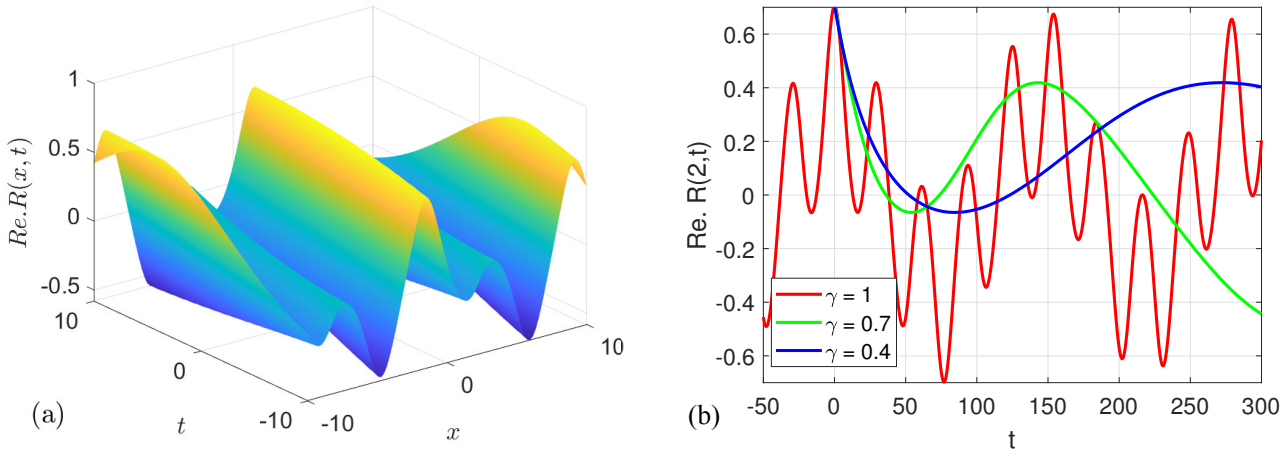


Figure 4. Graphic representation of the real part of the solution (29). (**a**) The 3D representation and (**b**) 2D representation for different values of the fractional order derivative.

6. Perturbed System

We now turn to the autoresonance behavior of the non-autonomous oscillator, wherein the system can self-synchronize with a slowly varying periodic excitation. To incorporate external driving, we augment the original model (1) with a specific time-periodic forcing function $\alpha_0 e^{iz}\mathrm{cn}(\beta\rho,\nu)$. The driven system then takes the form

$$i\,{}_n\mathbb{D}_t^{\gamma,\nu}\,R + R_{xx} + 2\mu\,R|R|^2 + m\,{}_n\mathbb{D}_t^{\gamma,\nu}(R_x) - \alpha_0 e^{iz}\mathrm{cn}(\beta\rho,\nu) = 0. \tag{35}$$

Physically, the added perturbation term represents an external time-periodic excitation acting on the wave envelope, such as a driven electromagnetic field in plasma media or an imposed modulation in optical fiber systems. Its amplitude and frequency quantify the strength and temporal rate of this external driving, which can be tuned experimentally. Including this term converts the autonomous Hamiltonian model into a non-autonomous driven system, enabling the description of resonance, quasi-periodic responses, and the onset of chaotic dynamics arising from the interaction between the medium's intrinsic oscillations and the external forcing.

Applying the transformation (2) and performingthe same procedures as in Section 2, we obtain

$$\begin{aligned}\Omega' &= \mathrm{Y},\\ \mathrm{Y}' &= \ell_1\Omega^3 - \ell_2\Omega + \alpha\mathrm{cn}(\beta\rho,\nu),\\ \kappa' &= \beta,\end{aligned} \tag{36}$$

where ℓ_1 and ℓ_2 are given by (8) and α is introduced instead of α_0 for simplicity as $\alpha = \frac{\alpha_0(p_1q_2+p_2q_1)}{p_2(p_1p_2q_2-p_2^2q_1-q_2^2)}$. The parameters α and β denote, respectively, the forcing amplitude and frequency of the external periodic drive. In what follows, we shall call (36) the perturbed system.

The analysis of periodic and chaotic dynamics of the wave behavior to the model (1) is complicated by a four-parameter space: the model parameters ℓ_1 and ℓ_2, together with the forcing parameters α and β that define the external perturbation.

We examine the unperturbed system (9) or the perturbed system (36) in the limit where the amplitude of external periodic forcing vanishes. Choosing the parameter set

$$p_1 = 0.3,\ p_2 = 0.03,\ q_1 = 1.859556098,\ q_2 = 0.7,\ \mu = 0.2390496318,\ m = -2.565967537, \tag{37}$$

we obtain $\ell_1 = -5.2$ and $\ell_2 = 19.05$. For the initial condition $(Y(0), \Omega(0)) = (0.1, 0.137066112)$, the constant a is evaluated from Equation (11) as $a = 0.09558$. Hence, $(\ell_1, \ell_2, a) \in \mathbb{R}^- \times \mathbb{R}^+ \times \mathbb{R}^+$. Following the bifurcation analysis, the perturbed system exhibits periodic dynamics, as confirmed by the two-dimensional and three-dimensional phase portraits and by the time series of Ω versus ρ shown in Figure 5a–c.

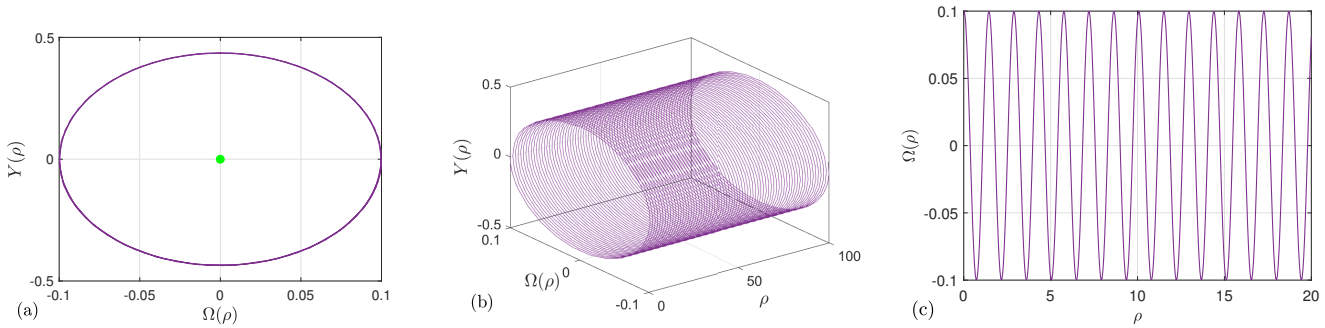


Figure 5. The behavior of the unperturbed system Equation (9) with initial conditions $(Y(0), \Omega(0)) = (0.1, 0.1370661118)$ and parameter values of $p_1 = 0.3, p_2 = 0.03, q_1 = 1.859556098, q_2 = 0.7$, $\mu = 0.2390496318, m = -2.565967537$. (**a**) 2D phase orbit; (**b**) 3D phase orbit; (**c**) Time series of $Omega(ho)$ against ho.

We now investigate the impact of an external periodic forcing on the dynamics of the unperturbed system (9). The analysis is carried out in two stages: first, by varying the forcing amplitude while keeping the frequency constant; and second, by altering the frequency while maintaining a fixed amplitude.

For this study, we adopt the parameter values given in Equation (37) and assume the forcing frequency is fixed at $\beta = 3$, while the amplitude α is allowed to vary. When the amplitude is set to $\alpha = 100$, the perturbed system (36) exhibits quasi-periodic behavior, as illustrated by the 2D and 3D phase portraits and the time series of Ω versus ρ in Figure 6a–c. This phenomenon occurs because the ratio of the interacting frequencies is incommensurable. Conversely, when the amplitude of the external forcing is increased to $\alpha = 200$ while the frequency remains fixed at $\beta = 3$, the system transitions to chaotic dynamics, as shown in Figure 7a–c.

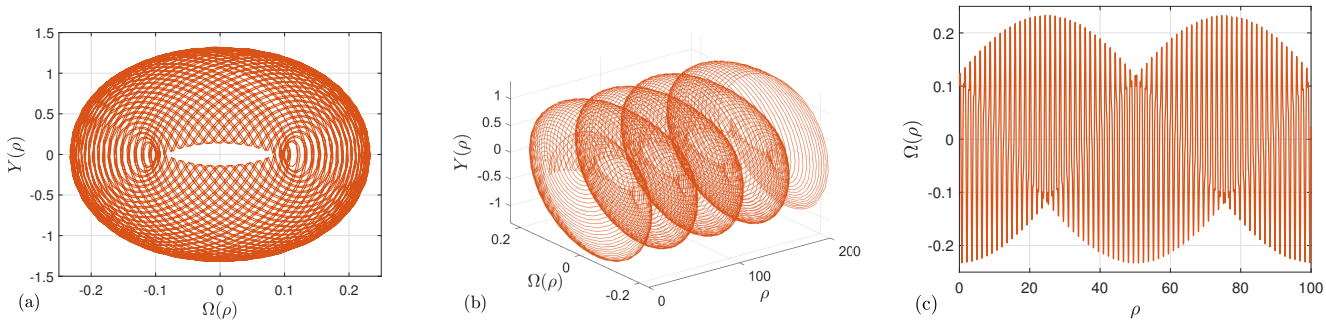


Figure 6. The behavior of the perturbed system Equation (36) with initial conditions $(Y(0), \Omega(0)) = (0.1, 0.1370661118)$ and frequency $\beta = 3$, amplitude $\alpha = 100$. Parameter values of $p_1 = 0.3$, $p_2 = 0.03$, $q_1 = 1.859556098, q_2 = 0.7, \mu = 0.2390496318, m = -2.565967537$. (**a**) 2D phase orbit; (**b**) 3D phase orbit; (**c**) Time series of $Omega(ho)$ against ho.

We proceed to evaluate the Lyapunov exponents for the perturbed system described in Equation (36), using the same parameter set as in Figure 7. Numerical evaluation of these exponents provides a powerful tool for detecting both the onset of chaos and the stability properties of nonlinear dynamics. However, proper interpretation of the results requires a solid understanding of the system's fundamental behavior, since the exponents

depend strongly on specific features of the model under study [40]. In practical terms, Lyapunov exponents serve as indicators of dynamical regimes: a positive value denotes chaotic motion, while a negative value reflects convergence toward stable trajectories.

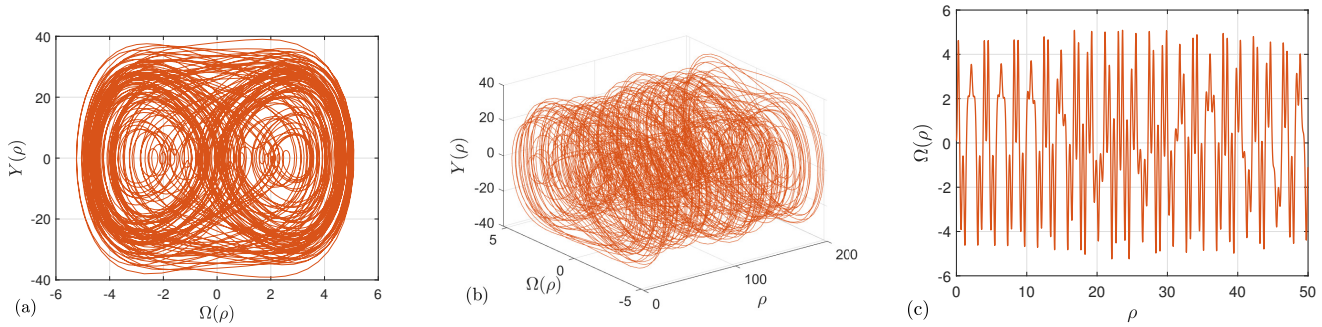


Figure 7. The behavior of the perturbed system Equation (36) with initial conditions $(\mathrm{Y}(0), \Omega(0)) = (0.1, 0.1370661118)$ and frequency $\beta = 3$, amplitude $\alpha = 200$. Parameter values of $p_1 = 0.3$, $p_2 = 0.03$, $q_1 = 1.859556098, q_2 = 0.7, \mu = 0.2390496318, m = -2.565967537$. (**a**) 2D phase orbit; (**b**) 3D phase orbit; (**c**) Time series of $Omega(ho)$ against ho.

For the system (36) with the parameter set (37), the Lyapunov exponents are

$$\lambda_1 = 0.07550652, \qquad \lambda_2 = -0.07550652, \qquad \lambda_3 = 0.00.$$

Figure 8 illustrates the convergence of the Lyapunov exponents. The presence of the positive Lyapunov exponent λ_1 confirms the chaotic behavior of the perturbed system (36).

Consequently, the transition to chaos under increased forcing amplitude α mirrors physical scenarios where strong external modulation—such as intense RF heating in plasmas or high-power periodic pumping in fibers—leads to wave turbulence, mode competition, or signal breakdown.

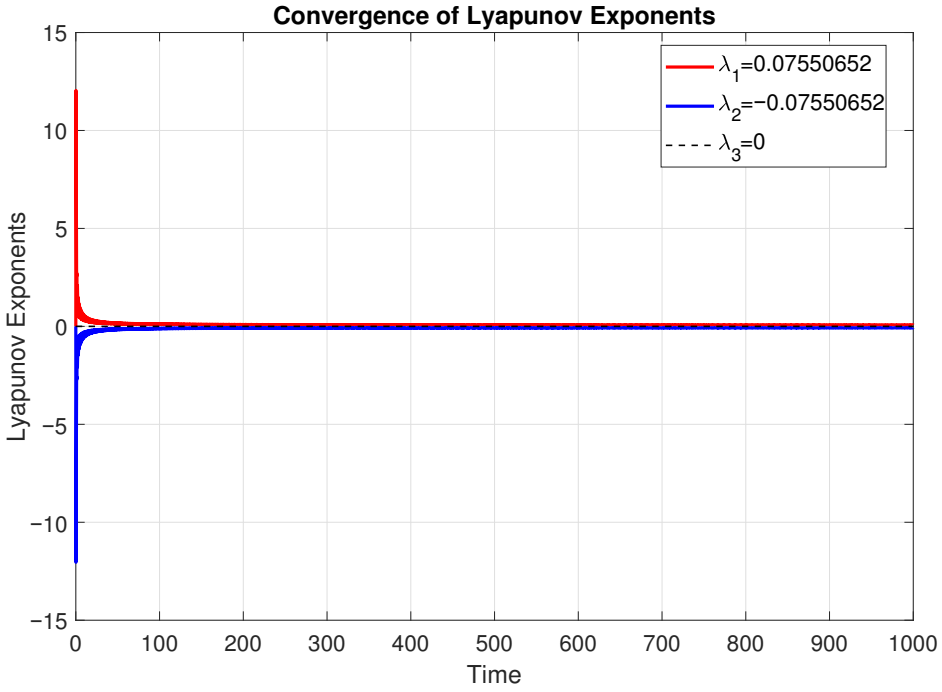


Figure 8. Lyapunov exponents for the perturbed system (36).

7. Conclusions

This study focuses on the qualitative dynamics of the modified unstable time-fractional nonlinear Schrödinger equation (mUNLSE), a model relevant to nonlinear wave propagation in plasma and optical fiber media. Through an appropriate transformation, the mUNLSE is reformulated as a conservative autonomous dynamical system. The resulting system is identified as a one-dimensional Hamiltonian framework. The equilibrium points are determined, and their stability is analyzed using the Lagrange theorem for Hamiltonian systems. A phase portrait is constructed and briefly discussed to illustrate the system's behavior.

By integrating the conserved quantity along intervals of real propagation, several exact solutions of the mUNLSE are obtained. The validity and consistency of these solutions are examined through the degeneracy property, which corresponds to studying the transition of solution types across phase-plane trajectories. Selected solutions are presented graphically to highlight their structural features.

Furthermore, the role of the fractional derivative order in shaping amplitude, localization, and dispersion is investigated through numerical simulations, emphasizing the memory effects inherent in fractional dynamics. An external periodic forcing is also introduced, transforming the mUNLSE into a perturbed non-autonomous dynamical system. The system's response to periodic driving is explored, revealing transitions from regular periodic motion to quasi-periodic and chaotic regimes. These behaviors are illustrated using two- and three-dimensional phase portraits as well as time-series analysis, with Lyapunov exponent calculations providing further confirmation.

We compare our results with those presented in two earlier studies, namely [41,42]. Arshad et al. [41] used a modified extended mapping method to analyze the fractional mUNLSE, constructing bright/dark solitons, combined dark–bright solitons, elliptic-function solutions, and periodic solitary waves under particular parameter conditions. Similarly, Zulfiqar and Ahmad [42] utilized the Exp-function approach to derive trigonometric, hyperbolic, and hybrid solutions for the mUNLSE, yielding bright/dark solitons, solitary waves, and periodic structures. In contrast, bifurcation analysis appears in other recent studies such as [43], though these typically overlook the critical intervals of real wave propagation essential for solution construction. Moreover, such works often assume trigonometric cosine perturbations, whereas our study employs Jacobi-elliptic forcing functions that more naturally emerge from the underlying dynamical system.

Overall, the findings enrich the theoretical understanding of fractional Schrödinger-type equations and shed new light on complex nonlinear wave phenomena in plasma physics and optical fiber systems.

Author Contributions: Conceptualization, M.M.E.-D. and A.A.E.; methodology, A.A.A., M.M.E.-D. and A.A.E.; software, A.A.E. and A.A.A.; validation, M.M.E.-D., A.A.E. and A.A.A.; formal analysis, M.M.E.-D. and A.A.E.; investigation, A.A.E. and A.A.A.; resources, A.A.E.; writing—original draft preparation, A.A.A., M.M.E.-D. and A.A.E.; writing—review and editing, M.M.E.-D.; project administration, M.M.E.-D.; funding acquisition, M.M.E.-D. All authors have read and agreed to the published version of the manuscript.

Funding: This Project was funded by the Deanship of Scientific Research (DSR) at King Abdulaziz University, Jeddah, Saudi Arabia under grant no. (IPP: 969–130-2025). The authors, therefore, acknowledge with thanks the DSR for technical and financial support.

Data Availability Statement: The original contributions presented in this study are included in the article. Further inquiries can be directed to the corresponding author.

Acknowledgments: The authors acknowledge the Deanship of Scientific Research (DSR) at King Abdulaziz University, Jeddah, Saudi Arabia, for the financial support.

Conflicts of Interest: The authors have no conflicts of interest.

Appendix A. Truncated *M*-Fractional Differentiation

To ensure this article is self-contained, we begin by presenting the essential definitions and fundamental ideas related to truncated *M*-fractional differentiation.

The truncated *M*-fractional derivative operator was introduced to overcome certain drawbacks of classical fractional operators, particularly regarding the validity of rules such as the chain, product, and quotient rules, as well as the mean value theorem. This operator is constructed based on the Mittag-Leffler function.

Definition A1 ([44]). *The truncated Mittag-Leffler function with one parameter, denoted by* $M_\delta^n(r)$*, is given by*

$$M_\delta^n(r) = \sum_{s=0}^{n} \frac{r^s}{\Gamma(\delta s + 1)}, \tag{A1}$$

where $\delta > 0$ *and* $r \in \mathbb{C}$.

Next, we introduce a specific form of the truncated *M*-fractional derivative of order p.

Definition A2 ([44]). *Let* $M_\delta^n(r)$ *be the truncated Mittag-Leffler function with* $\delta > 0$*, and let* $h : \mathbb{R}^+ \to \mathbb{R}$ *be a real-valued function with* $0 < \gamma < 1$*. The truncated M-fractional derivative of order* γ *for* h *is defined as*

$$ {}_nD^{\gamma,\nu}(h(t)) = \lim_{\eta \to 0} \frac{h\left(t\, M_\delta^n(\eta t^{-\gamma})\right) - h(t)}{\eta}, \tag{A2}$$

for all $t > 0$.

The main properties of the truncated *M*-fractional derivative are summarized below.

Theorem A1 ([44]). *Let* f_1 *and* f_2 *be functions that are truncated M-fractional differentiable of order* p *for* $t > 0$*, and let* $a_1, a_2 \in \mathbb{R}$*. Then the following rules hold:*

1. ${}_nD^{\gamma,\nu}(a_1h_1 + a_2h_2)(t) = a_1\, {}_nD^{\gamma,\nu}h_1(t) + a_2\, {}_nD^{\gamma,\nu}h_2(t)$,
2. ${}_nD^{\gamma,\nu}(t^q) = \dfrac{q}{\Gamma(\nu+1)} t^{q-\gamma}$, *for all* $q \in \mathbb{R}$,
3. ${}_nD^{\gamma,\nu}(h_1h_2)(t) = h_1(t)\, {}_nD^{\gamma,\nu}h_2(t) + h_2(t)\, {}_nD^{\gamma,\nu}h_1(t)$,
4. ${}_nD^{\gamma,\nu}\left(\dfrac{h_1}{h_2}\right)(t) = \dfrac{1}{h_2^2(t)}\left(h_2(t)\, {}_nD^{\gamma,\nu}h_1(t) - h_1(t)\, {}_nD^{\gamma,\nu}h_2(t)\right)$,
5. ${}_nD^{\gamma,\nu}(b) = 0$, *where* b *is a constant*,
6. ${}_nD^{\gamma,\nu}(h)(t) = \dfrac{t^{1-\gamma}}{\Gamma(\gamma+1)} \dfrac{dh(t)}{dt}$, *for differentiable* h,
7. ${}_nD^{\gamma,\nu}(h_1 \circ h_2)(t) = h_1'(h_2(t))\, {}_nD^{\gamma,\nu}h_2(t)$, *provided* h_1 *is differentiable at* $h_2(t)$.

The truncated *M*-fractional derivative adopted here differs from classical fractional operators in several ways. The Caputo derivative is defined via a power-law kernel, which is singular at the origin and is particularly suited for problems with physically interpretable initial conditions. The Caputo–Fabrizio derivative uses an exponential kernel, which is non-singular and often preferred for modeling processes with fading memory, such as viscoelasticity [45,46]. In contrast, the truncated *M*-fractional derivative is based on a truncated Mittag-Leffler kernel, allowing it to interpolate between classical fractional operators and integer-order calculus while preserving standard differentiation rules. This makes it especially convenient for constructing exact solutions and performing bifurcation analysis in nonlinear wave equations, as demonstrated in this work. However, like all fractional

operators, its physical interpretation depends on the context: in plasma and optical fiber models, it captures memory and hereditary effects that power-law or exponential kernels may describe differently. The choice of operator thus reflects a trade-off between analytical convenience, physical fidelity, and the specific memory structure of the system under study.

References

1. Gepreel, K.A. Exact soliton solutions for nonlinear perturbed Schrödinger equations with nonlinear optical media. *Appl. Sci.* **2020**, *10*, 8929. [CrossRef]
2. Zobeiry, N.; Humfeld, K.D. A physics-informed machine learning approach for solving heat transfer equation in advanced manufacturing and engineering applications. *Eng. Appl. Artif. Intell.* **2021**, *101*, 104232. [CrossRef]
3. Raza, N.; Ullah, M.A. A comparative study of heat transfer analysis of fractional Maxwell fluid by using Caputo and Caputo–Fabrizio derivatives. *Can. J. Phys.* **2020**, *98*, 89–101. [CrossRef]
4. Sgura, I.; Lawless, A.S.; Bozzini, B. Parameter estimation for a morphochemical reaction-diffusion model of electrochemical pattern formation. *Inverse Probl. Sci. Eng.* **2019**, *27*, 618–647. [CrossRef]
5. Jornet, M. Modeling of Allee effect in biofilm formation via the stochastic bistable Allen–Cahn partial differential equation. *Stoch. Anal. Appl.* **2021**, *39*, 22–32. [CrossRef]
6. Kaplan, M.; Ozer, M.N. Multiple-soliton solutions and analytical solutions to a nonlinear evolution equation. *Opt. Quantum Electron.* **2018**, *50*, 2. [CrossRef]
7. Malik, S.; Kumar, S.; Das, A. A (2+1)-dimensional combined KdV–mKdV equation: Integrability, stability analysis and soliton solutions. *Nonlinear Dyn.* **2022**, *107*, 2689–2701. [CrossRef]
8. Wróblewski, M. Nonlinear Schrödinger approach to European option pricing, author=Wróblewski, Marcin. *Open Phys.* **2017**, *15*, 280–291. [CrossRef]
9. Arora, G.; Rani, R.; Emadifar, H. Numerical solutions of nonlinear Schrodinger equation with applications in optical fiber communication. *Optik* **2022**, *266*, 169661. [CrossRef]
10. Liu, X.z.; Yu, J. A nonlocal nonlinear Schrödinger equation derived from a two-layer fluid model. *Nonlinear Dyn.* **2019**, *96*, 2103–2114. [CrossRef]
11. Shi, L.; Zhou, X. Exact solutions of a coupled space-time fractional nonlinear Schrödinger type equation in quantum mechanics. *Results Phys.* **2022**, *42*, 105967. [CrossRef]
12. Salas, A.H.; El-Tantawy, S.A.; Castillo H., J.E. The hybrid finite difference and moving boundary methods for solving a linear damped nonlinear Schrödinger equation to model rogue waves and breathers in plasma physics. *Math. Probl. Eng.* **2020**, *2020*, 6874870. [CrossRef]
13. Omote, M.; Sakagami, M.; Sasaki, R.; Yamanaka, I. Solvable quantum field theories and polynomial conserved quantities for the quantum nonlinear Schrödinger equation. *Phys. Rev. D* **1987**, *35*, 2423. [CrossRef]
14. Rizvi, S.T.; Seadawy, A.R.; Mustafa, B.; Ali, K.; Ashraf, R. Propagation of chirped periodic and solitary waves for the coupled nonlinear Schrödinger equation in two core optical fibers with parabolic law with weak non-local nonlinearity. *Opt. Quantum Electron.* **2022**, *54*, 545. [CrossRef]
15. Manukure, S.; Booker, T. A short overview of solitons and applications. *Partial Differ. Equ. Appl. Math.* **2021**, *4*, 100140.
16. Zhang, S. A generalized auxiliary equation method and its application to the (2+1)-dimensional Korteweg–de Vries equations. *Comput. Math. Appl.* **2007**, *54*, 1028–1038. [CrossRef]
17. Elmandouh, A.; Aljuaidan, A.; Elbrolosy, M. The integrability and modification to an auxiliary function method for solving the strain wave equation of a flexible rod with a finite deformation. *Mathematics* **2024**, *12*, 383. [CrossRef]
18. Malik, S.; Hashemi, M.S.; Kumar, S.; Rezazadeh, H.; Mahmoud, W.; Osman, M. Application of new Kudryashov method to various nonlinear partial differential equations. *Opt. Quantum Electron.* **2023**, *55*, 8. [CrossRef]
19. Elbrolosy, M.; Elmandouh, A. Painlevé analysis, Lie symmetry and bifurcation for the dynamical model of radial dislocations in microtubules. *Nonlinear Dyn.* **2025**, *113*, 13699–13714. [CrossRef]
20. Kumar, S.; Malik, S.; Rezazadeh, H.; Akinyemi, L. The integrable Boussinesq equation and it's breather, lump and soliton solutions. *Nonlinear Dyn.* **2022**, *107*, 2703–2716. [CrossRef]
21. Li, L.; Duan, C.; Yu, F. An improved Hirota bilinear method and new application for a nonlocal integrable complex modified Korteweg-de Vries (MKdV) equation. *Phys. Lett. A* **2019**, *383*, 1578–1582. [CrossRef]
22. Alhami, R.; Alquran, M. Extracted different types of optical lumps and breathers to the new generalized stochastic potential-KdV equation via using the Cole-Hopf transformation and Hirota bilinear method. *Opt. Quantum Electron.* **2022**, *54*, 553. [CrossRef]
23. Rezazadeh, H.; Neirameh, A.; Eslami, M.; Bekir, A.; Korkmaz, A. A sub-equation method for solving the cubic–quartic NLSE with the Kerr law nonlinearity. *Mod. Phys. Lett. B* **2019**, *33*, 1950197. [CrossRef]

24. Rehman, H.U.; Ullah, N.; Imran, M. Optical solitons of Biswas-Arshed equation in birefringent fibers using extended direct algebraic method. *Optik* **2021**, *226*, 165378. [CrossRef]
25. El-Dessoky, M.; Elmandouh, A. Qualitative analysis and wave propagation for Konopelchenko- Dubrovsky equation. *Alex. Eng. J.* **2023**, *67*, 525–535. [CrossRef]
26. Elmandouh, A. Nonlinear Dynamical Analysis of a Diffusion-Driven Bacterial Density Model: Integrability and Bifurcation Analysis. *Mathematics* **2025**, *13*, 3623. [CrossRef]
27. Elmandouh, A. Bifurcation, Quasi-Periodic, Chaotic Pattern, and Soliton Solutions to Dual-Mode Gardner Equation. *Mathematics* **2025**, *13*, 841. [CrossRef]
28. Rafiq, M.H.; Jhangeer, A.; Raza, N. The analysis of solitonic, supernonlinear, periodic, quasiperiodic, bifurcation and chaotic patterns of perturbed Gerdjikov–Ivanov model with full nonlinearity. *Commun. Nonlinear Sci. Numer. Simul.* **2023**, *116*, 106818. [CrossRef]
29. Ahmidi, M.; Mokni, K.; Ch-Chaoui, M. Influence of Prey Harvesting on the Dynamics of a Prey–Predator System: Multi-Parameter Bifurcation Analysis. *Nonlinear Dyn.* **2025**, *113*, 31841–31870. [CrossRef]
30. Lamb, G.L. *Elements of Soliton Theory*; Wiely: New York, NY, USA, 1980.
31. Roshid, M.M.; Uddin, M.; Boulaaras, S.; Osman, M. Dynamic optical soliton solutions of M-fractional modify unstable nonlinear Schrödinger equation via two analytic methods. *Results Eng.* **2025**, *25*, 103757. [CrossRef]
32. Ahmad, J.; Anwar, M.; Mustafa, Z. Nonlinear wave dynamics of fractional unstable and modified unstable nonlinear Schrödinger equations through analytical solutions. *J. Opt.* **2025**, *54*, 2112–2130. [CrossRef]
33. Arshad, M.; Seadawy, A.R.; Lu, D. Optical soliton solutions of the generalized higher-order nonlinear Schrödinger equations and their applications. *Opt. Quantum Electron.* **2018**, *50*, 421. [CrossRef]
34. Seadawy, A.R. Modulation instability analysis for the generalized derivative higher order nonlinear Schrödinger equation and its the bright and dark soliton solutions. *J. Electromagn. Waves Appl.* **2017**, *31*, 1353–1362. [CrossRef]
35. Arshad, M.; Seadawy, A.R.; Lu, D. Exact bright–dark solitary wave solutions of the higher-order cubic–quintic nonlinear Schrödinger equation and its stability. *Optik* **2017**, *138*, 40–49. [CrossRef]
36. Tala-Tebue, E.; Seadawy, A.R.; Djoufack, Z. The modify unstable nonlinear Schrödinger dynamical equation and its optical soliton solutions. *Opt. Quantum Electron.* **2018**, *50*, 380. [CrossRef]
37. Seadawy, A.R.; Iqbal, M.; Lu, D. Construction of soliton solutions of the modify unstable nonlinear Schrödinger dynamical equation in fiber optics. *Indian J. Phys.* **2020**, *94*, 823–832. [CrossRef]
38. Goldstein, H. *Classical Mechanics*; Addison-Wesley Series in Physics; Addison-Wesley: Boston, MA, USA, 1980.
39. Gantmacher, F. *Lectures in Analytical Mechanics*; Mir Publishers: Moscow, Russia, 1975.
40. Layek, G. *An Introduction to Dynamical Systems and Chaos*; Springer: New Delhi, India, 2015; Volume 1.
41. Arshad, M.; Seadawy, A.R.; Lu, D.; Jun, W. Modulation instability analysis of modify unstable nonlinear schrodinger dynamical equation and its optical soliton solutions. *Results Phys.* **2017**, *7*, 4153–4161. [CrossRef]
42. Zulfiqar, A.; Ahmad, J. Soliton solutions of fractional modified unstable Schrödinger equation using Exp-function method. *Results Phys.* **2020**, *19*, 103476. [CrossRef]
43. Harun-Or-Roshid; Abdeljabbar, A.; Uddin, M.S.; Khatun, M.S. Phase portraits and orbit wise dynamics solutions, quasi-periodic and chaotic behavior of heisenberg ferromagnetic spin chains mode. *Partial Differ. Equ. Appl. Math.* **2025**, *13*, 101044. [CrossRef]
44. Sousa, J.V.D.C.; de Oliveira, E.C. A new truncated *M*-fractional derivative type unifying some fractional derivative types with classical properties. *Inter. J. Anal. Appl.* **2017**, *16*, 83–96.
45. Podlubny, I. *Fractional Differential Equations: An Introduction to Fractional Derivatives, Fractional Differential Equations, to Methods of Their Solution and Some of Their Applications*; Elsevier: Amsterdam, The Netherlands, 1998; Volume 198.
46. Caputo, M.; Fabrizio, M. A new definition of fractional derivative without singular kernel. *Prog. Fract. Differ. Appl.* **2015**, *1*, 73–85.

Disclaimer/Publisher's Note: The statements, opinions and data contained in all publications are solely those of the individual author(s) and contributor(s) and not of MDPI and/or the editor(s). MDPI and/or the editor(s) disclaim responsibility for any injury to people or property resulting from any ideas, methods, instructions or products referred to in the content.